X-LPNHE 95/4
March 1995

The Plasma Beat-Wave Acceleration Experiment at Ecole Polytechnique

Submitted to Nucl. Instr. and Meth. **A**

F. Amiranoff[1], J. Ardonceau[2], M. Bercher[3], D. Bernard[3], B. Cros[6], A. Debraine[3], J. M. Dieulot[3], J. Fusellier[5], F. Jacquet J. M. Joly[5], M. Juillard[5], G. Matthieussent[6], P. Matricon[3], P. Miné[3], B. Montès[3], P. Mora[4], R. Morano[3], J. Morillo[2], F. Moulin[1], P. Poilleux[3], A. E. Specka[3], C. Stenz[7]

X-LPNHE 95/4

[1]LULI, [2]SESI, [3]LPNHE, [4]CPHT; all: Ecole Polytechnique, 91128 Palaiseau, France
[5]DSM-DAPNIA-SEA CEA Saclay, 91191 Gif sur Yvette, France
[6]LPGP, Université Paris Sud, 91405 Orsay, France
[7]GREMI, Université d'Orléans, 45000 Orléans, France

Abstract

We present an experiment for demonstrating the principle of plasma beat-wave acceleration. The beating of two Nd-laser pulses creates a relativistic plasma wave in a deuterium plasma. Electrons at an energy of 3 MeV are injected into the plasma. We observe several hundred electrons accelerated up to 3.7 MeV.

This paper is mainly devoted to the description of the experimental apparatus. In the design of the apparatus, we gave particular attention to efficient electron injection and to background noise suppression. We present also some preliminary results of electron acceleration experiments.

1 Introduction

Among new methods to accelerate particles by high electric fields, the plasma beat-wave technique [1] has been investigated by several groups over the last decade. In this scheme, two high-intensity laser pulses are focused in a gas, and create a fully ionized plasma. The light intensity modulation associated with the beating of the two laser waves provides a longitudinal ponderomotive force – which oscillates at the frequency difference of the two laser waves – on the plasma electrons. If this frequency difference is equal to the natural plasma frequency, an electron plasma wave is resonantly excited.

Provided that the laser frequencies are much higher than the plasma frequency, the phase velocity of the longitudinal plasma wave is equal to the mean group velocity of the light waves in the plasma, i.e., close to the speed of light.

The longitudinal electric field associated with the charge separation of the plasma wave can reach up to several GV/m. The plasma wave amplitude grows with time until it reaches saturation because of various possible mechanisms. A relativistic particle injected with the right phase can catch the wave and gain energy.

It has been demonstrated that injected electrons could be accelerated up to several MeV, using a two-frequency CO_2 laser with wavelengths of about 10 μm [2, 3]. The acceleration of background plasma electrons with the same technique has also been reported [4]. In these experiments, the saturation of the plasma wave is attributed to relativistic de-tuning [5].

In the experiment at Ecole Polytechnique presented here, a two frequency Neodymium laser with wavelengths of about 1 μm is used. In a first step, we investigated the plasma creation by the laser via multi-photo-ionization of the gas [6]. Subsequently, we studied the creation of the relativistic plasma wave by the beating of two laser pulses [7]. In contrast to CO_2 laser experiments, the peak amplitude $\delta n/n$ of the relativistic plasma wave is limited here by modulational instability: The beat-wave-generated plasma wave couples to ion density perturbations and decays into non-relativistic daughter electron waves. The measured value of $\delta n/n$ (1 to 5 %) has been found to be in agreement with model predictions (1.5%) of the peak amplitude of the plasma wave in the presence of modulational instability [8]. The measured amplitude corresponds to an electric field between 0.3 and 1.5 GV/m.

Following this optical study of the beat-wave generated plasma wave, we prepared the injection of electrons into the plasma. The new experimental set-up designed for

that purpose is described in the main body of this paper (section 2). Recently, we have observed acceleration of electrons by a plasma beat-wave: some preliminary results are presented in section 3.

2 Experimental set-up

2.1 Overview

The design of the experimental set-up for the electron acceleration experiments was governed by two major goals: an efficient electron injection and a high signal-to-noise ratio. The reduction of background noise, mainly originating from scattered, non-accelerated electrons, is a primary concern in this experiment, because the time constant of the detector (5 ns) is much larger than the duration of the signal. The latter is of the same order of magnitude as the lifetime of the plasma waves, which we estimate to 40 ± 20 ps from the duration of the Thomson scattering signal.

The lay-out of the experimental set-up is shown in figure 1. A laser beam is focused into a gas vessel, and creates a plasma at the focus. An electron beam is injected into the gas vessel through a thin aluminium window, and is then deflected and focused on the plasma by a triple focusing magnet. The electron spot is precisely monitored at the entrance window and at the plasma location using optical transition radiation (OTR) imaging. In particular, we align the relative positions of the laser and electron foci by the use of one single monitor. A quadrupole-dipole magnetic spectrograph analyses the accelerated electrons in momentum. These are then counted in a calorimeter hodoscope made up of scintillators read by photomultiplier tubes. The non-accelerated electrons are ejected to a beam dump.

2.2 Laser injection, plasma creation, and optical diagnostic

The laser system is similar to the one used in preceeding experiments [7]. Two laser pulses delivered by Nd-YAG and Nd-YLF oscillators are amplified with a time delay of 1 ns in the laser chain of LULI up to an energy of 4.4 ± 0.2 J and 11.8 ± 0.4 J respectively, and with an output diameter of 90 mm. The YAG (YLF) pulse at wavelength 1.064 μm (1.053 μm) is 200 ± 10 ps (90 ± 10 ps) long (FWHM). The quoted errors correspond to typical shot-to-shot variations within a series.

The experimental area is located near the electron source and at a distance of about 190 m from the laser. The laser beam is guided inside a vacuum pipe (0.04 mbar) to preserve the quality and the stability of the beam. An optical relay made of a pair of 50 m focal length lenses images the entrance window to the exit. The beam is steered inside the pipe by two pairs of motorized dielectric mirrors. The mirror holders are mounted on massive concrete blocks, and are thus mechanically decoupled from the vibrations of the beam pipe. The beam position can be monitored at eight different locations along the beam path. Each monitor is made up of a retractable cardboard reflector imaged by a CCD camera. The mirrors, the monitors, and the vacuum system are remotely controlled by a single personal computer.

Profile and focal spot measurements show that the beam quality is preserved in the transport. The short-term (1 min.) stability of the beam position at the focus of a 1.5 m focal length lens is of the order of 10 μm (RMS), which matches our needs. At larger time-scales, we observe a slow drift of typically 0.1 mm/h, which is probably due to thermal deformations of the buildings. Therefore, we re-align the laser beam between successive shots.

The two pulses are synchronized in the experimental area with rotating plates and polarizers. They are then focused by a 1.5 m focal length doublet lens, and enter the gas vessel through a BK7 window. The focal spot is imaged with high magnification on a CCD camera, and has a diameter of 60±20 μm (FWHM). The alignment system of the laser beam, of the electron beam, and of the plasma wave diagnostics is different from the one used in previous experiments [9], and is described in section 2.6.

The laser focus presents a central spot surrounded by several diffraction rings. We estimate that about half of the energy is contained in the central spot, and that the peak intensity is close to 10^{15} W/cm^2, which is much larger than the ionization threshold of deuterium. Thus, the gas is fully ionized by multi-photo-ionization [6], and the initial electron density of the plasma is equal to twice the molecular density of the gas. The resonant electron density is $(1.115 \pm 0.026) \cdot 10^{17}\text{cm}^{-3}$, corresponding to a deuterium pressure of 2.27 ± 0.05 mbar at 22^0C. The systematic error on the resonant electron density is determined by the accuracy of the measurement of the two oscillator wavelengths.

In contrast to previous experiments [7], we observe here the Thomson scattering at 5^0 of the incoming near-infrared (*not* frequency doubled) laser light on the plasma waves [8]. A system consisting of a grating spectrograph, a streak camera, and a CCD camera gives time and frequency resolved measurements of the scattered light. The unshifted laser light is blocked by an interference filter in front of the spectrograph and by a neutral density filter in the analysing plane of the spectrograph. Thus, we observe only one Thomson scattering satellite.

2.3 Electron source

The electrons with a kinetic energy of 2.5 MeV are provided by a Van de Graaff accelerator, which is ordinarily used for solid state physics. As we inject a small pencil of test electrons into a plasma of about 0.1 mm in diameter, we have characterized the beam with high precision using OTR monitors (see 2.6). The results of this study have led to several modifications of the electron line. In particular, the energy of the beam oscillates slowly over several seconds with a peak-to-peak amplitude of about 10 keV, which would lead to an inadmissible transverse beating of the electron beam of 2 mm. Consequently, we have designed a new, dispersionless beam line.

We have also discovered that the alternative magnetic field created by the motor driving the belt of the Van de Graaff deflects the beam at a frequency of 50 Hz. As it occurs at some distance from the filament, this deflection appears at subsequent waists as a rotation of the spot in the transverse plane with an amplitude of a fraction of a millimetre. Magnetic shielding of the motor reduces the amplitude of the rotation by

one order of magnitude. The residual movement is suppressed by pulsing the electron source at 10 Hz with an adapted phase locking. The pulse length can be varied, and is set to 0.4 ms with a peak intensity of 315 ± 15 μA. During the experiment, the laser shots are fired on the rising slope of the electron pulse at an intensity of about 200 μA.

The measured emittance ϵ of the electron beam — defined as the product of the RMS beam size and the RMS divergence at a location of zero correlation — is equal to 0.06 mm·mrad.

2.4 Injection of the electrons into the gas vessel

The gas vessel with a fill pressure of about 2 mbar has to be separated from the vacuum in the beam pipe (10^{-6} to 10^{-5} mbar) by a thin window. The elastic scattering of the low energy electrons on their passage through the entrance window has two main effects: First, multiple low angle scattering increases the beam divergence, and hence affects the injection into the plasma. This also causes several inconveniences for the design of the whole experimental set-up. In particular, the air-gap of the magnets must be large, and their aberrations must be further minimized. Second, single large-angle scattering creates a halo around the "Gaussian core", which may generate considerable background noise in the detector.

For these reasons we had to give particular attention to the choice of the window material and thickness. Because of the very high irradiation dose rate on the window (3 MGy /ms with a focused beam), a metallic foil must be used. We chose aluminium for its low atomic number, and because it can be easily mounted vacuum-tight. The thickness is chosen as a compromise between electron scattering considerations on the one hand, and the pressure resistance of the foil and its porosity on the other hand. The measured gas conductance through a 1.5 μm thick foil, used here, with a diameter of 4 mm is lower than 10^{-7} l/s, providing a tolerable relative pressure drop rate smaller than $5 \cdot 10^{-6}$ per hour.

Scattering of the electrons by the entrance window

Multiple scattering of charged particles traversing matter is usually described by the "Molière" formula [10], which gives the RMS width of the Gaussian core of the scattering angle distribution[1].

Since the mean number of collisions per unit length n is rather small (3.8 μm^{-1} for Al), we checked the result of the Molière formula with a Monte Carlo simulation of plural scattering. The width of the angular distribution is estimated from the angle that contains 68% of the events ("68%-width"), and is equal to 8.9 mrad, whereas the Molière value is 8.7 mrad, and the measured value is 7 ± 1 mrad.

The large angle behaviour can be described by the approximation of one large scattering event. The probability of a scattering angle larger than η is then : $P(\theta > \eta) = n \cdot t \cdot (\theta_c/\eta)^2$, where θ_c is the cut angle from screening ($\theta_c = 3$ mrad for Al).

[1] A window thickness of the order of one micron, envisaged here, is about two orders of magnitude out of the given validity range of the Molière formula [11].

The fraction of electrons that are intercepted by an aperture stop behind the window grows linearly with the window's thickness t. For a 1.5 μm thick Al window, the fraction outside a cone with half apex angle of 60 mrad is calculated to be 1.3% in comparison to 1.5% as computed with the Monte Carlo. For an incoming intensity of 200 μA, this number corresponds to $1.6 \cdot 10^4$ e^-/ns.

These simple considerations show that a huge number of the incoming electrons is scattered at angles larger than six times the width of the angular distribution. If not collimated properly, a large fraction of these are back-scattered from the vessel walls, and may create background noise in the detector. Therefore, an optimized collimation system has been designed (see 2.8).

Focusing of the electron beam on the entrance window

The increase of the beam divergence by the entrance window degrades the beam emittance. The blow-up of the emittance is minimized by a suitable choice of the beam optics.

The angular divergence of the beam beyond the window is simply $\sigma'_\theta = ({\sigma_\theta}^2 + {\sigma_D}^2)^{1/2}$, where σ_θ is the RMS angular divergence of the incoming beam, and σ_D is the RMS scattering angle.

After crossing the foil, the beam has a different waist, which may be virtual (fig. 2). Its width σ' can be written: $\sigma' = [\sigma^2 + x^2 {\sigma_\theta}^2 {\sigma_D}^2/({\sigma_\theta}^2 + {\sigma_D}^2)]^{1/2}$, where σ is the width of the waist of the incoming beam and x is the waist-to-window distance. Obviously, the minimization of σ' leads us to focus the beam on the window ($x = 0$), and we get $\sigma' = \sigma$. This corresponds to a beam emittance behind the window: $\epsilon' = \sigma' \sigma'_\theta = \sigma({\sigma_\theta}^2 + {\sigma_D}^2)^{1/2} = \epsilon(1 + (\sigma_D/\sigma_\theta)^2)^{1/2}$. Consequently, we minimize the emittance blow-up by focusing the beam as strongly as possible on the window.

In the experimental area, a quasi-parallel beam with a width of about 1 mm is received and focused on the entrance window by a magnetic solenoid lens. The lens-to-window distance cannot be smaller than 317 mm because of space constraints. This implies that $\sigma_\theta \approx 3$ mrad, and $\sigma \approx 20$ μm. In this case, we may use the approximation of a thick window ($\sigma_\theta \ll \sigma_D$), and we obtain: $\sigma'_\theta \approx \sigma_D = 9$ mrad, and $\epsilon' = \epsilon \cdot \sigma_D/\sigma_\theta = 0.18$ mm·mrad.

The x dependence of σ' reduces to: $\sigma' = [\sigma^2 + x^2 \sigma_\theta^2]^{1/2}$. Accordingly, the longitudinal focus position must be adjusted to better than $\delta_x = \sigma/\sigma_\theta = 7$ mm, which is easily achieved even in presence of energy fluctuations. The precision required for the measurement of the size of the focal spot is of the order of σ, and is attained using the OTR beam monitors.

2.5 Injection magnet

After crossing the window, the beam is brought on the laser axis by a bending magnet, which also images the entrance waist on the plasma. In order to obtain a stable spot, the magnet has to be non-dispersive (achromatic).

Instead of an achromatic magnet combination, we use a single "triple focusing", i.e., stigmatic and achromatic, dipole magnet, in order to minimize the path of the

electrons in the gas. The path has to be as short as possible, since any electron scattered by a gas molecule between the entrance window and the plasma is imaged outside the plasma.

Magnet calculation

The optics of a homogeneous-field dipole magnet is usually described by the following parameters [12]: the drift length before (after) the magnet A (B), the radius of curvature R of the electrons, the angle of the central ray with the entrance (exit) face of the dipole α (β), and the deflection angle φ (fig. 3). All quantities of dimension length can be normalized to the radius of curvature, and are in this case denoted by a small letter, e.g. $a = A/R$. Hence, the set (a,b,φ,α,β) defines a dipole magnet.

Let (O, x, y, z) be the moving frame of the central ray, in which (Ox) is the tangent, (Oy) the normal, and (Oz) the bi-normal, and s is the curvilinear coordinate. The plane (Oxy) is called the median or horizontal plane of the magnet, and the direction of the magnetic field (Oz) is called the vertical direction. The angles are written $y' = \mathrm{d}y/\mathrm{d}x$, and the momentum deviation $\Delta p/p$ is denoted δ. In the paraxial approximation, the particle coordinates $(y_2, y_2', z_2, z_2', \delta)$ at $s = s_2$ are linear functions of the entrance coordinates at $s = s_1$. The elements of the transfer matrices are written in short form, e.g. $(y|y) = \mathrm{d}y_2/\mathrm{d}y_1$.

In this notation, a triple focusing magnet is described by the system of equations: $[(y|y') = 0\ ,\ (z|z') = 0\ ,\ (y|\delta) = 0]$, where each matrix element depends on the five parameters defining the dipole. The two remaining free parameters can be chosen to be the ratio of the two arms $g = b/a$ and φ.

The solution of the system of equations leads to a second-degree polynomial equation in a [13]. At fixed positive g, the equation has one physical solution ($a > 0$, $b > 0$) for $232^0 > \varphi > 180^0$ and two physical solutions for $360^0 > \varphi > 232^0$. The two branches of solutions correspond respectively to magnets having either no or exactly one intermediate focal point in the vertical plane.

The spot size on the entrance window is well matched to the plasma width. Consequently, we choose $g = 1$, and we obtain a symmetrical magnet with $a = b$, $\alpha = \beta$, and unit magnification in y and z. Furthermore, we choose $\varphi = 270^0$ to get reasonable values of a and α. This choice also minimizes the second order aberrations, and allows an easy implementation in the lay-out. Solving the above system of equations, we obtain $a = b = 2$ and $\alpha = \beta = \arctan(1/2) \approx 26.6^0$.

The above results are obtained in the limit of a small air-gap. In practice, however, the magnet has a large air-gap H, which is in our case at least equal to $2{\cdot}\theta_{\mathrm{coll}}{\cdot}A$, where $\theta_{\mathrm{coll}} = 60$ mrad is the collimation angle (see 2.8), i.e., $H > 0.24{\cdot}R$. For mechanical reasons we must use an air-gap as large as $H = 0.6{\cdot}R$. This affects the fringe field and hence vertical focusing. The shape of the fringe field is calculated by solving numerically Poisson's equation [14]. Finally, the magnet is fine-tuned using a ray-tracing program [15], and we end up with a still symmetric dipole magnet with $\varphi = 270^0$, $a = b = 2.91$, and $\alpha = \beta = 33.2^0$ (fig. 4).

Optical properties of the injection magnet

The radius of curvature R is chosen so as to minimize the broadening of the beam spot by elastic scattering in the gas. We can minimize this broadening either by reducing the number of scatterings, or by reducing their effect at the plasma.

In deuterium gas at 2 mbar, the values of the elastic scattering parameters defined in (2.4) are $\theta_c = 1.3$ mrad and $n = 0.42$ m^{-1}. The typical transverse position of a scattered electron at the plasma is $A\cdot\theta_c$, and is of the order of the size of the waist σ' in absence of gas for $R \approx \sigma'/(a\theta_c) = 8$ mm, which is obviously too small to be feasible. The fraction of the electrons undergoing no scattering is $\exp(-(a+\varphi+b)R\cdot n)$, which is smaller than 68% for $R < 0.1$ m. For this chosen value of R, the typical transverse position of a scattered electron at the plasma is 260 μm. Thus, the main part of the 32% scattered electrons forms a large, low-density halo around the plasma, which is invisible on the monitors. Yet when the scattering occurs close to a waist, the position at the plasma can be rather small: These scatterings contribute to the width of the waist. The simulation shows that the 68%-width of the waist increases from 25 to 38 μm.

The aberrations δ_y and δ_z of the injection magnet are dominated by the second and third order terms in the horizontal and vertical angles:

$$\delta_y = R\cdot(C_y^{02}\cdot z'^2 + C_y^{12}\cdot y'\cdot z'^2) \qquad \text{and} \qquad \delta_z = R\cdot(C_z^{03}\cdot z'^3 + C_z^{21}\cdot y'^2\cdot z'),$$

where the aberration coefficients are equal to $C_y^{02} = -0.7$ rad^{-2}, $C_z^{03} = -70$ rad^{-3}, $C_y^{12} = 51$ rad^{-3}, and $C_z^{21} = -44$ rad^{-3}.
Likewise, the aberrations create a halo of electrons as far as 1.5 mm from the plasma (for a collimation at $\theta_{\text{coll}} = 60$ mrad), but their contribution to the 68%-width of the beam is rather small: 5.4 μm horizontally and 7.8 μm vertically.

Taking into account the above effects, we expect an RMS width of the electron beam at the plasma close to 40 μm.

Beam test of the injection magnet

During the commissioning of the magnet we adjusted five parameters: the position and the angle of the beam in the horizontal plane, its horizontal and vertical focus at the plasma location, and the dispersion of the magnet. This has been done by adjusting the following control variables: the position of the magnet in the horizontal plane, the magnetic field inside the magnet, the height of the field clamps, and the index of the magnet. The latter acts only on the stigmaticity of the magnet, and can be tuned in a small range ($\pm 2\%$) by printed circuits carrying a current sheet.

The beam spot at the plasma location is monitored by an OTR monitor. The typical values of the RMS widths are 27 μm (H), 24 μm (V) in vacuum and 47 μm (H), 41 μm (V) in 2 mbar of deuterium (fig. 5), and are compatible with the above estimations. The stability of the beam is of the order of 10 μm (RMS), which matches our needs.

2.6 Beam monitoring and alignment

The position and the size of the electron beam are measured in four different locations by beam monitors. These monitors exploit the optical transition radiation (OTR) emitted by the electrons impinging on a metal surface (*radiator*) to image the beam spot on a CCD camera [16, 17].

When a charged particle crosses the boundary between two media with different refractive indexes, such as the surface of a metal foil, it emits electromagnetic radiation. In the case of a metal-to-vacuum transition (forward TR), the emitted spectrum may range from the infrared to the X-ray domain, whereas in the inverse case (backward TR) the emission takes place mainly in the visible (OTR).

The backward emission is maximal on a cone centred on the direction of specular reflection of the electron, with a half apex angle of γ^{-1}, where γ is the Lorentz factor of the particle (fig. 6). This property permits easy observation of the beam at rather large angles. Therefore, the radiator is tilted by an angle ψ with respect to the beam axis. As the total photon yield is of the order of magnitude of the fine structure constant ($\approx 1/137$), which is rather small, the angle of observation χ is chosen at a maximum of emission. The working distance t_0 between the optical system with magnification m and the metal surface is determined by available space.

#	ψ	χ	$\lvert m \rvert$	t_0 [mm]	NA
1	15^0	40^0	1	200	0.093
2	17.5^0	45^0	1	260	0.090
3	17.5^0	45^0	1	200	0.093
4a	37^0	87^0	1/34	760	0.011
4b	37^0	87^0	1/25	300	0.017

Table 1: Geometrical and optical parameters of the beam monitors

The first monitor (see table 1) controls the size and the position of the beam on the entrance window, which is used as the radiator. The second monitor views the beam spot at the plasma location. The radiator, a 13 μm thick Al foil, is mounted on a retractable target holder. The latter is also equipped with the secondary collimator of the upstream collimation system and with a silica prism used for the alignment of the Thomson-scattering diagnostic. The second monitor is used to adjust the relative positions of the electron focus and of the laser focus. The monitor optics is located outside the cone of specular reflection of the laser, and collects only diffusely reflected light from the mat foil. Thus, the laser focus at the nominal plasma location and the focus of the monitor optics can be adjusted independently.

A third monitor with a radiator 3 cm behind the plasma is used for angular measurements. The optical system and the camera are located above the median plane of the experiment, and are thus omitted in figure 1.

The functions of these three monitors require a high spatial resolution of the order of 10 μm, which is well matched to the pixel size of the CCD (8×16 μm^2).

This resolution is achieved by using a symmetric optical system with unit magnification, made up of two identical achromatic doublets. The computed value of the resolution, defined as the RMS width of the point spread function, is in good agreement with the measured values (fig. 7). At large apertures, the spherical aberration dominates, whereas at lower apertures diffraction becomes important. (We define here the diffraction limit as the RMS size of the central spot of the Airy pattern for $\lambda = 500$ nm.) We use only the green part (480–560 nm) of the large OTR spectrum in order to make the contribution of secondary chromatism negligible.

When viewing the laser spot on the second monitor, we have to refocus in the near infra-red. For this purpose, the CCD camera is mounted on a motorized stage.

Two further monitors (4a and 4b) are used for the test and calibration of the electron spectrograph. We use the exit window (Al, 0.5 mm) as the radiator. The large viewing field is imaged with low magnification by ordinary TV lenses.

The sensitivity of the monitors can be defined as the product of the current density of the faintest visible beam spot and of the integration time of the CCD (20 ms). We measure a visibility threshold of 0.1 μA (monitor 1) for a focused spot ($\sigma = 20$ μm), which gives a sensitivity of 0.8 $\mu C \cdot mm^{-2}$.

2.7 Magnetic electron spectrograph

The accelerated electrons are analysed in momentum by a magnetic spectrograph. The design of the spectrograph was governed by a number of competing specifications. In particular, it must be broad-range (3–6 MeV/c) and stigmatic at 3 MeV/c. Furthermore, it must possess a high angular acceptance to match the high divergence of the accelerated electrons ($\approx$ 50 mrad RMS, [18]). It must also have convenient geometrical properties, i.e., a straight focal line, a "narrow fan" of central rays, and a reasonably low incidence angle on the focal line to permit correct functioning of the electron detector.

We started out with the search for an optimal single dipole magnet but, for geometrical reasons, we opted for an optically equivalent quadrupole-dipole (QD) combination, which was then further optimized [17].

The spectrograph images the object point, i.e., the plasma, on the entrance of the beam dump to ensure an efficient ejection of the non-accelerated electrons. The stigmaticity condition: $(y|y') = 0$, and $(z|z') = 0$ at $p = 3$ MeV/c fixes the arms a and b of the dipole, the same notations as in section 2.5 being used here. Again, the solution of this system of equations leads to a second-order polynomial equation in a.

The demand for a suitable beam geometry has led us to consider the particular type of dipoles, for which the entrance point is located in the (extended) exit face (Fowler-Elbek dipoles [19]). For these magnets, the deflection angle φ of the central ray does not depend on momentum, and the fan of central rays is parallel on exit. This fixes the exit angle: $\beta = (\varphi - \pi)/2$.

We then adjust the remaining parameters α and φ so as to minimize the first-order vertical astigmatism at momenta $p > 3$ MeV/c, and to minimize the incidence angle γ_F on the focal line. Both a low value of the entrance angle α and of γ_F cannot

be attained with a single dipole. A large α is undesirable for magneto-optical reasons and because of space limitations.

Therefore, vertical focusing is accomplished by a quadrupole instead of an inclined entrance face of the dipole. The latter can now be perpendicular to the central ray ($\alpha = 0$). The QD-combination is then further optimized for a finite air-gap using a ray-tracing program [15]. Figure 8 shows the ray-tracing of the spectrograph in the horizontal and vertical planes for electrons at 3, 4, 5 and 6 MeV/c and for marginal rays at $\pm$100 mrad.

The dimensionless dispersion is defined by $d = (y|\delta) = (\partial y/\partial p)\cdot(p/R)$. For Fowler-Elbek dipoles we find $d = 1 - \cos\varphi = 1.7$. We choose the radius of curvature R_0 of the 3 MeV/c electrons so as to reach a compromise between a sufficiently low smallest detectable momentum and a reasonable length of the focal line. Between the entrance of the dump and the first scintillator is a dead zone, which cannot be smaller than 40 mm for mechanical reasons. For the chosen value of $R_0 = 250$ mm, the smallest detectable momentum is 3.27 MeV/c, and the length of the focal line from 3 to 6 MeV/c is 54 cm.

At 3 MeV/c, the aberrations of the spectrograph are dominated by the second-order terms in the horizontal and vertical angles:

$$\delta_y = R\cdot C_y^{20}\cdot y'^2 \qquad \text{and} \qquad \delta_z = R\cdot C_z^{11}\cdot z'\cdot y' \ ,$$

where the aberration coefficients are equal to $C_y^{20} = -4.0$ rad^{-2}, and $C_z^{11} = -4.4$ rad^{-2}. The horizontal aberrations create a tail on the low energy side. This tail is cut by the down-stream collimation system at 8 mm from the central trajectory, as can be observed in the horizontal ray-tracing; in the vertical plane the tail extends to $\pm$ 10 mm. All these electrons enter the dump.

The resolution (RMS) of the spectrograph is determined by its aberrations; for a beam with a divergence of 50 mrad [18], it varies from 33 keV/c (at 3 MeV/c) to 28 keV/c (at 6 MeV/c), and is well matched to the granularity of the detector (158 keV/c).

During the beam test of the spectrograph, the beam with a divergence of 9 mrad was scanned along the exit window by varying the magnetic field in the dipole. The measured RMS widths are 1 mm and 0.9 mm in the y and z directions, which is in good agreement with the calculated resolution. The measured dispersion is compatible with the above calculation.

2.8 Collimation of stray electrons

We have seen above that the entrance window scatters a huge number of electrons at large angles and that many electrons undergo elastic scattering in the gas. Furthermore, electrons may be deflected by the radial electric field generated by the plasma wave ([2, 18]). These electrons eventually hit the walls of the chamber with a low incidence angle i and some of them are back-scattered.

We have studied the back-scattering of electrons on a wall with the program EGS4 [20], which simulates the electromagnetic interactions of elementary particles in matter. At normal incidence ($i = 0$), we get a back-scattering probability of 2.3% (Al) and 8.4% (Fe). Note that these values are about two times lower than

the experimentally measured values of 5% (Al) and 14% (Fe) [21], probably because EGS4 uses the Molière approximation for multiple scattering. The back-scattering probability rises drastically with increasing incidence angle (fig. 9), and almost reaches unity at grazing incidence. (In the latter case the exit probability is already 50% after the first Coulomb scattering.) Note also that the mean energy of the re-emitted electrons increases, and that their exit angle decreases with i. Many of these electrons propagate downstream in the chamber, and eventually create background noise in the detector.

Therefore, we have designed a collimation system to block the halo electrons before they hit the walls. A primary collimator is installed behind the foil and intercepts the electrons scattered at large angle. A secondary collimator is located around the plasma, and blocks the electrons scattered on the edge of the primary collimator. As the incident rate of electrons is large, their scattering on the edge of a collimator is studied in detail using EGS4.

A collimator is a plate of thickness e with a conical bore with angle ξ' and entrance radius R (fig. 10). The collimation angle ξ is the angle of incidence of the electrons on the edge. The scattering skin-depth of the edge is found to be a few tens of microns. Let $p(r)$ be the density distribution of the incident electrons on the front face of the collimator and $q(r)$ the probability of forward diffusion on the edge. Then, the fraction of forward scattered electrons is $f = \int q(r)p(r)dr$. As $p(r)$ does not vary significantly over the thin skin-depth, f becomes $p(R)\int q(r)dr = p(R)\varepsilon = 2{\cdot}n{\cdot}t{\cdot}\varepsilon{\cdot}\theta_c^2/(d{\cdot}\xi^3)$, where $\varepsilon = \int q(r)dr$ is an equivalent thickness. A quantity ε_0 similar to ε is defined for electrons crossing the image plane at less than the radius of the secondary collimator (4 mm).

The values of ε and especially ε_0 are very sensitive to the difference $\xi' - \xi$, which is called the freeing angle (fig. 11). For $\xi' < \xi$, the electrons are incident at low angles on the inner, conical surface of the collimator, and exit by the same face: the collimator acts as a scatterer. On the contrary, when $\xi' > \xi$, the electrons are incident on the front face, and the collimator is much more efficient, as expected. High Z materials scatter away grazing electrons more efficiently, and are thus favoured.

An "upstream" collimation system is installed before the plasma, and cleans the beam after the entrance window (fig. 12). A "downstream" collimation system cleans the beam after the plasma.

Upstream collimation system

The primary collimator u_1 is made of a 20 mm thick stainless steel plate with a collimation angle ξ of 60 mrad and a freeing angle of 10 mrad. We calculate a forward scattered flux from the edge of the primary collimator of 300 e^-/ns. The secondary, retractable, cylindrical collimator u_2 with a radius of 4 mm is located in the image plane of the injection magnet, around the plasma. The outcoming flux is then 1 e^-/ns. In view of the horizontal magnifications of the spectrograph, most of these electrons end up in the beam dump (cf. 2.7, 2.10).

Downstream collimation system

Another collimation system is installed downstream the plasma to block the electrons scattered at large angles in the plasma.

The first collimator d_1 is located in front of the quadrupole, shadowing the beam pipe. This collimator has an elliptical bore to leave clearance for the Thomson scattered light at 5^0. The collimation angle is 110 mrad in the vertical plane, 130 mrad in the horizontal plane, and the freeing angle is 10 mrad.

The second collimator d_2 is located between the quadrupole and the dipole, with a geometrical collimation angle of 130 mrad and a collimator angle of 300 mrad. It provides an efficient cut in the horizontal plane because of the defocusing action of the quadrupole. For the same reason the cut depends on energy.

A third "slit" S is located at an angle inside the dipole, and provides a cut at ± 15 mm in the vertical plane. It blocks electrons of 5 to 6 MeV with a relatively large vertical angle, which would otherwise hit the horizontal walls of the chamber.

Note that when the retractable secondary collimator of the upstream system is removed, the noise level in the detector is unchanged. Therefore, the downstream system acts as an efficient secondary system of the upstream one.

The efficiency of the downstream collimation system is tested by inserting the retractable foil at the plasma location. This increases the electron beam divergence up to a 68%-width of 35 mrad and generates a wide halo. However, the noise in the detector increases only by a factor of two.

Angular acceptance

The acceptance of the apparatus is limited by the downstream collimation system and by the height of the detector in conjunction with the vertical astigmatism of the spectrograph (fig. 13). We can see that the acceptance of the collimators at 3 MeV is larger than 80 mrad, i.e., larger than θ_{coll}. Therefore, the downstream collimation system works safely in the shadow of the upstream one.

In the energy range of the detector, the horizontal cut is close to 90 mrad. The vertical cut is equal to 110 mrad at low energies (3.27–3.41 MeV), and then decreases because of the limited height of the scintillators (3.41–4.84 MeV).

2.9 Electron counter

The accelerated electrons are detected in a calorimeter hodoscope composed of scintillators read by photomultiplier tubes (PMTs). The accelerated electrons impinge almost simultaneously on the scintillator, and leave all their kinetic energy in it. Thus, the signal constitutes a measurement of the number of electrons in the burst, provided that a precise energy calibration of each detector segment is done.

The detector is an array of 10 scintillators, each $2 \times 2.2 \times 5.8$ cm^3 in size, separated by 1 mm thick lead septa for containment. The positions of the axes of the scintillators correspond to an energy range from 3.34 to 4.77 MeV with a total energy range of 3.27 to 4.84 MeV.

We optimized the transverse dimensions of the scintillators and of the septa with a simulation using EGS4 [20], assuming here a right angle geometry, i.e., $\gamma_F = 0$. Figure 14 gives the mean percentage of energy lost in the scintillator, in the lead septum, and lost by back-scattering, as a function of the impact position of the electron. The longitudinal dimension of the scintillators is determined with a second simulation. In this simulation, the light rays are generated on the entrance face of the scintillator and tracked to the PMT photocathode, and the response uniformity is checked as a function of the origin of the photons.

The decay constant of the organic scintillator (NE111A) is 1.6 ns. The light is recorded by Hamamatsu R1635 PMTs, with a useful photocathode diameter of 8 mm and a rise time of 0.8 ns.

The pulse heights are measured by CAMAC-driven ADCs, triggered by the laser pulse. In order to take advantage of the short signal, we insert linear gate modules[22], with a gating time of 5 ns, between the PMTs and the ADCs. These gates are upgraded versions of linear gates originally developed for a different experiment [23].

We synchronize the detector channels with an attenuated laser pulse, sent directly on the PMTs. The energy dependence of the time of flight of accelerated electrons is accounted for by adapted cable lengths.

Calibration

The detector is calibrated by measuring cosmic muons, which deposit on average 4.4 MeV per event. The left peak in the pulse height spectrum represents background above discrimination, whereas the right peak is the muon peak (fig. 15). The energy calibration is cross-checked by observing the end spectrum of a ^{60}Co gamma source. Varying the high voltage applied to the PMTs and using fast amplifiers, we extend the dynamic range from one to a thousand electrons of 2.5 MeV kinetic energy.

The variation of the gain as a function of the high voltage is measured for each PMT, with a light emitting diode as the source, and found to follow very strictly a power law. The PMTs are operated at 900V and with an amplifier of gain 14 during the cosmic calibration runs, and at 555V and without amplifier during the physics runs. The signal amplitude is a few hundred millivolts, well below the impulse saturation of the PMTs, close to 1.5V.

2.10 Beam dump

As the lifetime of the plasma wave is rather short, only a small fraction of the incoming electrons is accelerated during the gated time interval. The non-accelerated electrons are directed into a beam dump where they are absorbed so as to generate as little as possible background noise in the detector.

The dump has the shape of a prismatic bottle with a bottom made of low Z material (aluminium (0.9 mm) and water) to minimize the number of back-scattered electrons (cf. 2.8), and backward-emitted γ rays.

Most of the hard γ's are emitted forward along the direction of the incident particles (fig. 16), and soft γ's are easily blocked with a lead shielding. The remaining

backward γ rate is computed with EGS4, and is equal to 1.2 ns^{-1} incident on each scintillator. Most of these photons do not interact in the detector.

The fraction of back-scattered electrons from water is 0.8% over a solid angle of 2π. With a simple bottle with a depth of 300 mm and a bottleneck area of 840 mm^2, 14 e^-/ns are re-injected into the chamber, and subsequently bent by the spectrograph into the detector. Moreover, low-angle back-scattering of electrons off the side-walls of the dump may increase this rate. Preliminary measurements had shown that this source of noise was dominating (2–10 e^-/ns per segment). Therefore, we have installed a magnetic no-return device, which bends the back-scattered electrons into the side-walls of the dump (fig. 1). This reduces the noise level of back-scattered electrons from the dump to less than 0.005 e^-/ns per segment.

The Čerenkov light generated by the beam in water is viewed by a TV camera through a silica window, and allows us to control the presence of the beam in the dump. A lead shielding protects the electron counter from external electron and γ noise.

2.11 Background noise level

The background noise level is the sum of various contributions, the e^- scattering in the gas, the e^- back-scattering and γ retro-emission from the dump, the e^- scattering, and γ emission on the edges of the collimators.

The sum of the four last contributions is measured under vacuum, and is very small: With a continuous electron beam of 0.1 ± 0.01 μA being injected into the vessel, the count rate at a discrimination threshold equivalent to 1 MeV is close to $2.5 \cdot 10^3$/s. This corresponds to a probability of $4 \cdot 10^{-9}$, and to a count rate of 0.005 e^-/ns at a beam current of 200 μA.

The dominating source of noise is the scattering of electrons in the gas. The probability density of the scattering angle per unit path length is calculated in the approximation of one large scattering event: $d^2p/(d\Omega \cdot ds) = n \cdot \theta_c^2/(\pi \cdot \theta^4)$. After a substitution of variables, we obtain the probability density per unit scintillator area as an integral over the curvilinear coordinate s. The integral contains the elements of the transfer matrix from the scattering location to the image plane. The obtained probability per segment decreases approximatively as the inverse of the fourth power of the dump-to-segment distance, as one would expect in the approximation of small segments. The corresponding count rate in the segment closest to the dump is 0.17 e^-/ns.

The observed rate is higher: 2 e^-/ns ($p = 1.6 \cdot 10^{-6}$) per segment, and increases slightly with the dump-to-segment distance. We believe that this gas-correlated noise is due to scattered electrons that impinge on the steel flange constituting the entrance of the dump. A fraction of $6.1 \cdot 10^{-4}$ of the beam is scattered on to the flange, 14% of these electrons are back-scattered, and the dipole bends part of them into the detector. This corresponds to a total back-scattered fraction of $8.5 \cdot 10^{-5}$. The observed rate in the whole detector is then about one fifth of the computed total rate, which seems reasonable.

3 Experimental operation and results

Before the experiment, the chamber is evacuated to 10^{-7} mbar by a diffusion pump and afterwards filled with deuterium gas. The gas density is measured with a precision of $3 \cdot 10^{-3}$, and is stable to 10^{-3} per day.

After an alignment of the beams, a series of "shots" at 12 minutes interval is started. About one minute before each shot, the positions of the electron spot and of the laser spot at the plasma location are finely adjusted and recorded. For each shot the laser energies, pulse durations, and YAG-YLF delay Δt are also recorded. The ADC measurements are acquired on a personal computer and stored. In addition, we view two channels on storage oscilloscopes. Pedestals are periodically recorded either with or without electrons.

The analysis of the data is still in progress, and complete results will be published elsewhere [24]. We present here only the results of a pressure scan.

For this scan, the calibration constants range from 1 to 3 electrons per ADC-count. An overall systematic uncertainty on the number of observed electrons is due to the calibration process ($\pm 15\%$), and is not shown in figures 19 and 20. The width of the pedestal of the first PMTs is of about 2 ADC-counts, both with and without electrons (fig. 17). The oscilloscope tracks show a beautiful single pulse above a very small noise (fig. 18). (The signal duration of 15 ns is due to the propagation of the signal in the cable from the detector to the oscilloscope.) The excellent correlation between the ADC and the oscilloscope measurements provides a cross-check of correct timing between the trigger of the linear gates and the signal of the PMTs.

The pressure scan shows a narrow peak near the resonant pressure (fig. 19), which proves the plasma beat-wave origin of the signal (shots #31 to #39, three shots with inadequate Δt being omitted). The signal is maximal at a pressure of about 2.3 mbar, which is compatible with the resonant pressure after temperature correction.

The measured energy spectrum of accelerated electrons at $P = 2.284$ mbar is compared in figure 20 to a 2D numerical simulation [18], using our experimental parameters. In this simulation, the plasma wave amplitude at each point in space is taken to be proportional to the laser intensity (not taking into account saturation). The peak amplitude of the plasma wave is taken to be $\delta n/n = 1.6\%$, as deduced from the end-point of the observed energy spectrum. We assume here a plasma wave amplitude ramping linearly with time (see fig. 6 in reference [8]). The simulation agrees with the experimental data for a ramping duration of 10 ps.

A series of null tests was also done: shots with either no electrons, or no gas, or only one laser wavelength, or combinations of these. None of these shots showed a signal of accelerated electrons.

4 Conclusion

We have presented the apparatus for an experiment demonstrating the principle of plasma beat-wave acceleration with a two-frequency Nd:glass laser. The two major design goals of the experimental set-up were the efficient injection of an electron beam of about 0.1 mm in diameter into a plasma of about the same width, and the maximal suppression of background noise.

The laser beam is brought to the experimental area by a transport system carefully designed to ensure beam stability. For the same reason, the existing electron beam line has been upgraded. The laser and electron beams are monitored at the plasma location by the same high precision monitor. The resulting uncertainty on the distance between the center of the electron spot, and the center of the plasma is then of the order of $10 - 20$ μm.

The reduction of background noise has governed the design of the whole experimental set-up. This has led to the choice of a single injection magnet with a large air-gap, and has imposed strong constraints on the design of the electron spectrograph. Furthermore, it has led to the dedicated design of a two-stage collimation system, of an adapted beam dump, and to the use of fast detectors. The resulting $S/\sqrt{N}$ ratio reaches 200.

We have observed the acceleration of externally injected electrons by a relativistic plasma wave. This is the first evidence of plasma beat-wave acceleration with a Nd:glass laser. The observed maximum energy gain is 0.7 MeV. A preliminary analysis, which does not take saturation effects into account, shows that this result is compatible with a peak plasma wave amplitude of about 1.6%, which agrees with previous optical measurements. The corresponding peak electric field is 0.5 GV/m.

5 Acknowlegments

We gratefully acknowledge the help of the staff of the LULI, LPNHE and SESI during the experiment. We thank also M. Poitevin, S. Simon, and Y. Fournier (DAPNIA) for their help with the modification of the electron beam line.

We thank F. Méot (LNS) who supplied us with his ray-tracing program, his assistance, and many invaluable hints on magnet design.

This work was financially supported by Ecole Polytechnique, IN2P3-CNRS, SPI-CNRS, CEA, EEC, and DRET.

References

[1] T. Tajima and J. Dawson, Phys. Rev. Lett. **43** (1979) 267.

[2] C.E. Clayton et al., Phys. Rev. Lett. **70** (1994) 37.
C.E. Clayton et al., Phys. Plasmas **1** (1994) 1753.
M. Everett et al., Nature **368** (1994) 527.

[3] N. A. Ebrahim, J. Appl. Phys. **76** (1994) 7645.

[4] Y. Kitigawa et al., Phys. Rev. Lett. **68** (1992) 48.

[5] F. Martin et al., New Developments in Particle Acceleration Techniques, CERN preprint 87-11.

[6] J.R. Marquès et al., Phys. Fluids B**5** (1993) 597.

[7] F. Amiranoff et al., Phys. Rev. Lett. **68** (1992) 3710.

[8] F. Moulin et al., Phys. Plasmas **1** (1994) 1318.

[9] F. Amiranoff et al., Rev. Sci. Instr. **61** (1990) 2133.

[10] Review of Particle Properties, Particle Data Group, Phys. Lett. B **204** (1988)

[11] G. R. Lynch, O. I. Dahl, Nucl. Instr. and Meth. **B58** (1991) 6-10.

[12] Deflecting Magnets H. A. Enge, in "Focusing of Charged Particles", edited by A. Septier, Academic Press, 1967.

[13] D. Bernard, A. E. Specka, *in preparation.*

[14] The CERN POISSON programe package (POISCR) Users guide, R.F. Holsinger, C. Iselin (available at CERN).

[15] ZGOUBI Users' Guide, F. Méot, S. Valéro, SATURNE note LNS/GT/93-12 (1993).

[16] A. E. Specka et al., proceedings of the IEEE Particle Accelerators Conference, pp. 2450-2452, Washington, D.C., 1993.

[17] A. E. Specka, Ph.D. thesis (*in French*), unpublished (1994).

[18] P. Mora, J. Appl. Phys. **71** (1992) 2087.

[19] D. J. Prowse, W. .M. Gibson, J. Sci. Instr. **33** (1956) 159.
J. Borggreen et al., Nucl. Inst. and Meth. **24** (1963) 1.

[20] The EGS4 code system, W. R. Nelson et al., SLAC-Report-265, December 1985.

[21] G. Soum et al., Revue Phys. Appl. **22** (1987) 1189-1209, *in French.*

[22] J.M. Dieulot et al., preprint LPNHE/X 94-11.

[23] J.M. Dieulot et al., Nucl. Instr. and Meth. A**314** (1992) 185.

[24] F. Amiranoff et al., *submitted to* Phys. Rev. Lett.

List of Figures

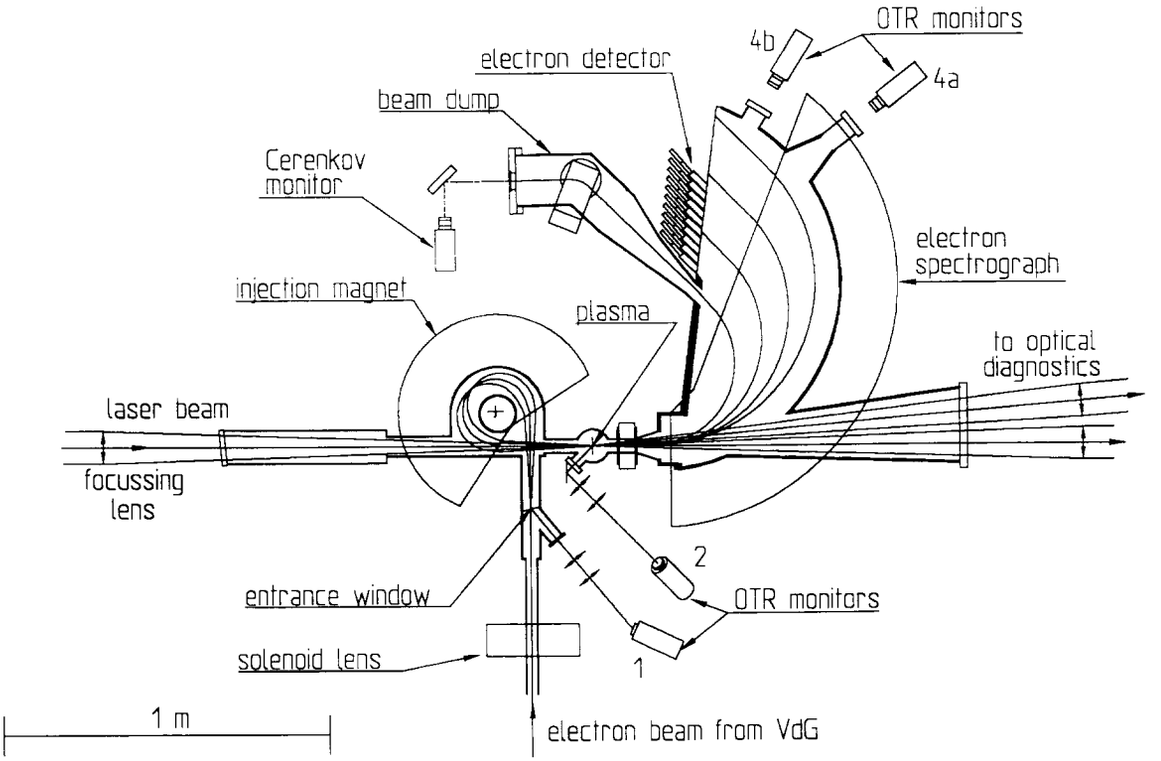

Figure 1: The lay-out of the experimental set-up.

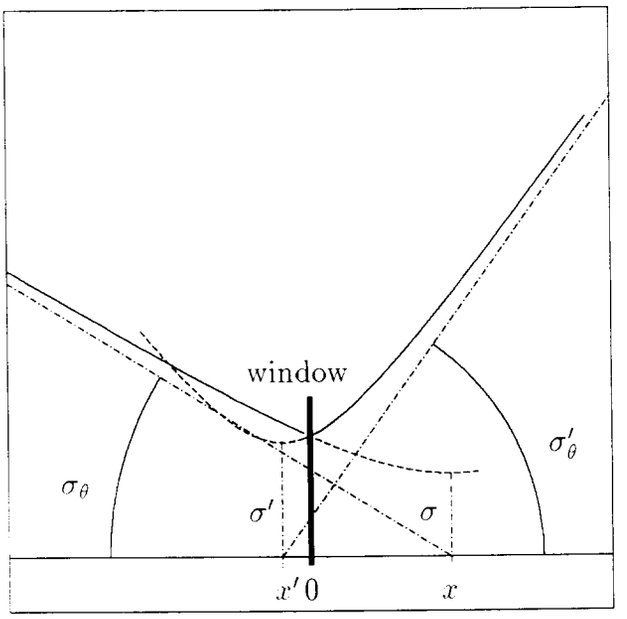

Figure 2: Focusing of the electron beam on the entrance window (see text).

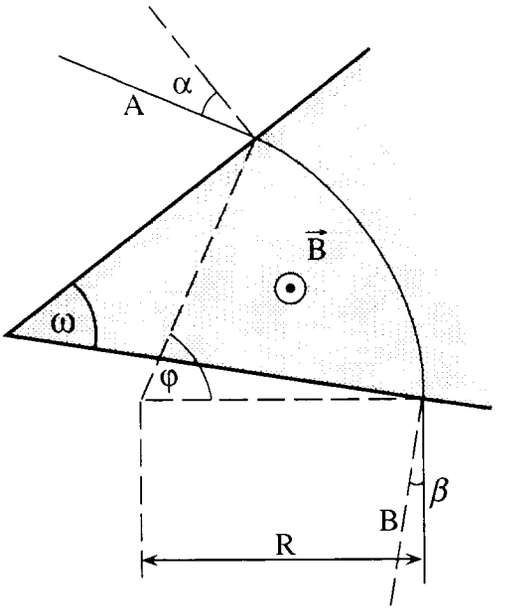

Figure 3: Dipole parameter definition.

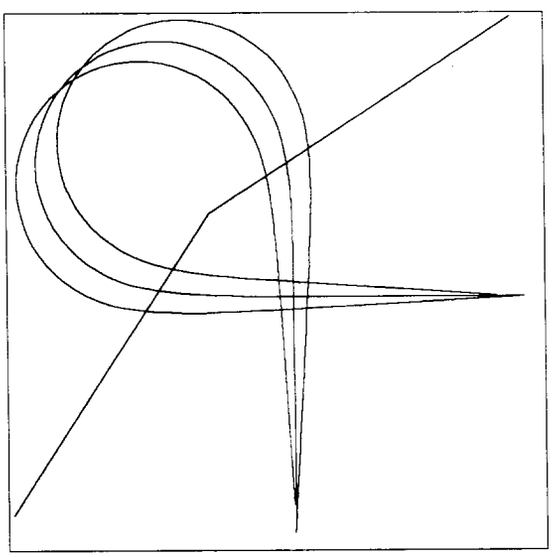

(a) Horizontal Focusing.

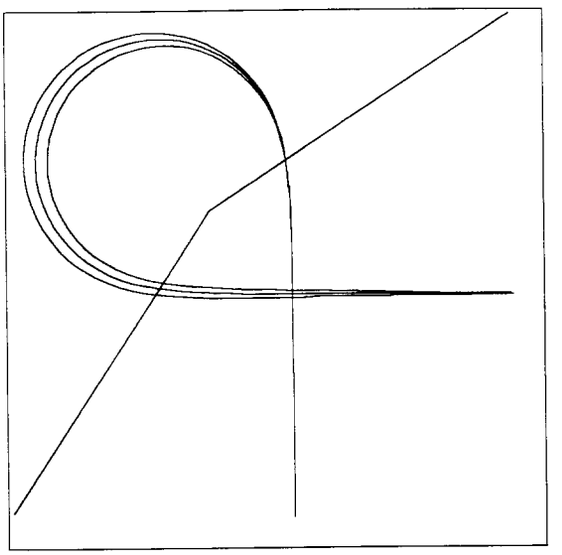

(b) Achromaticity.

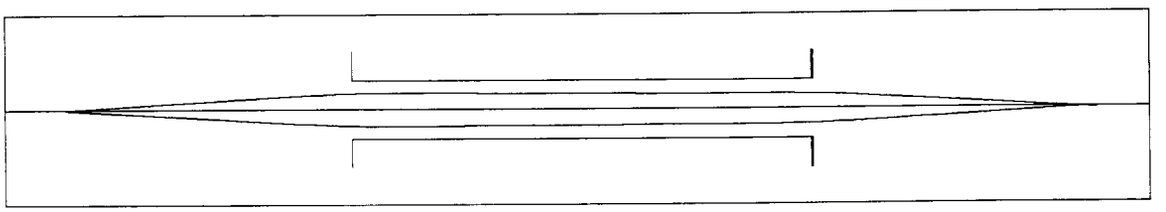

(c) Vertical focusing.

Figure 4: Optical properties of the injection magnet. The marginal electrons are emitted at the collimation angle θ_{coll} (see 2.8), and at a momentum deviation $\delta = \pm 0.05$.

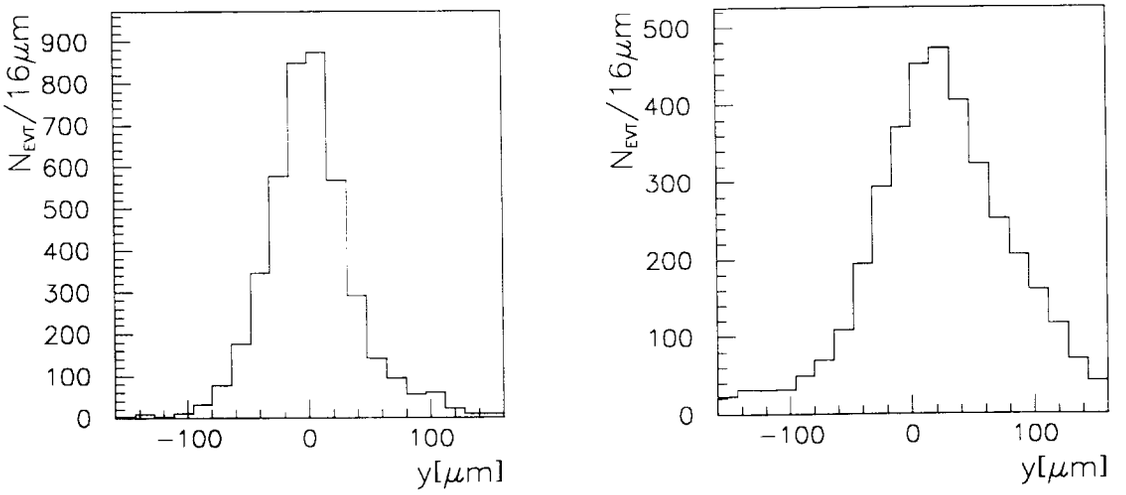

(a) vacuum.

(b) 2 mbar of deuterium.

Figure 5: The electron spot at the plasma location (horizontal plane).

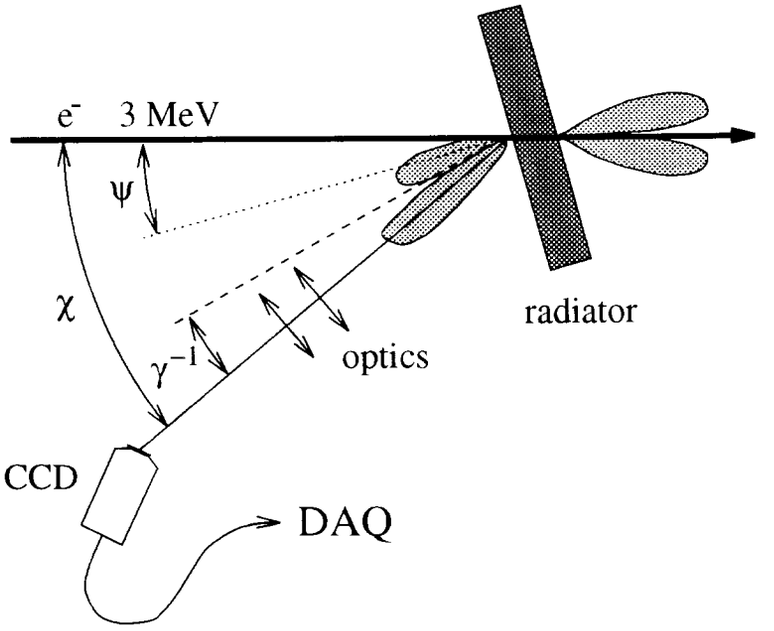

Figure 6: OTR monitor (schematic).

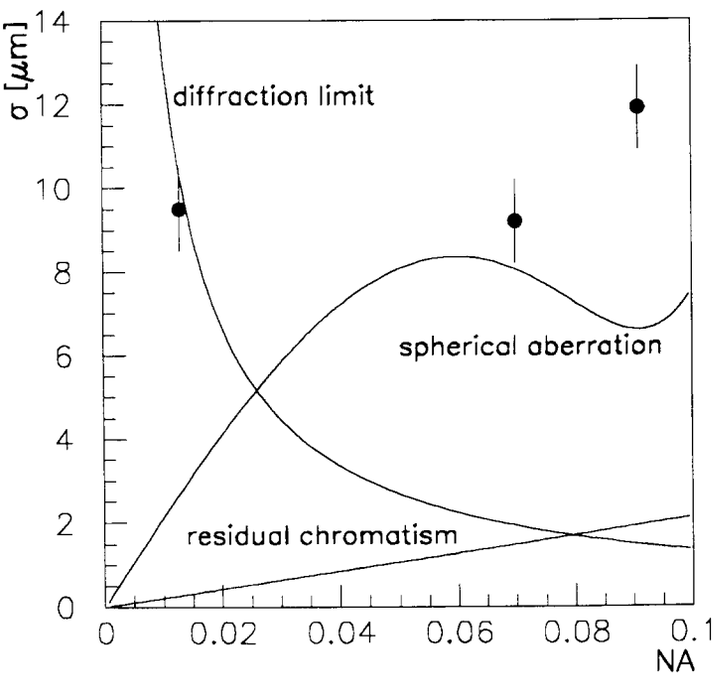

Figure 7: The resolution of the first monitor as a function of numerical aperture (controlled by a diaphragm) [17].

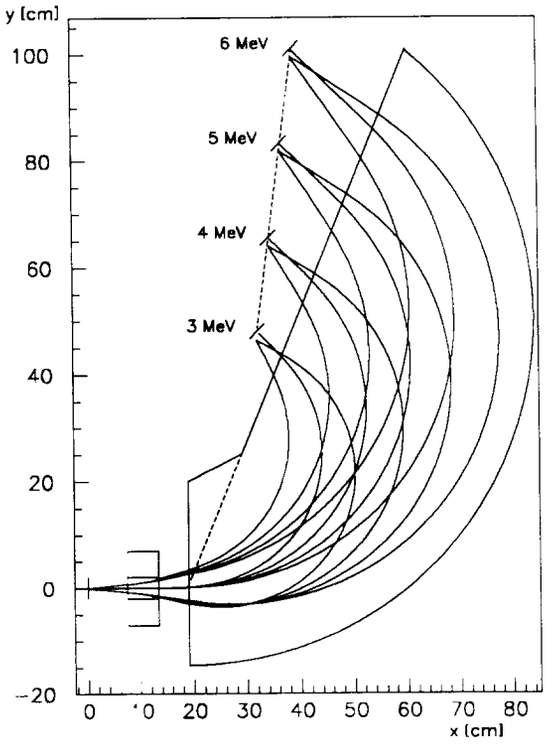

(a) horizontal ray-tracing.

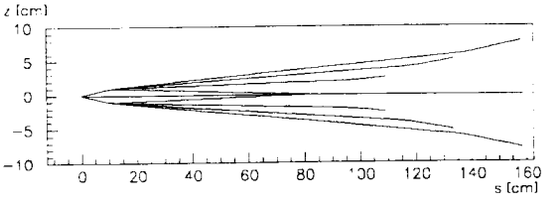

(b) vertical ray-tracing.

quadrupole		
length		60 mm
gradient		2.1 T/m
dipole		
magnetic field	B	0.04 T
radius (3 MeV/c)	R_0	250 mm
air gap	H	100 mm
entrance angle	α	0^0
deflection angle	φ	136^0
exit angle	β	-22^0
focal line incidence angle	γ_F	37^0
horizontal magnification		-0.34
vertical magnification		-8.2
focal line sagitta		0.15%

(c) numerical parameters.

Figure 8: Magnetic electron spectrograph.

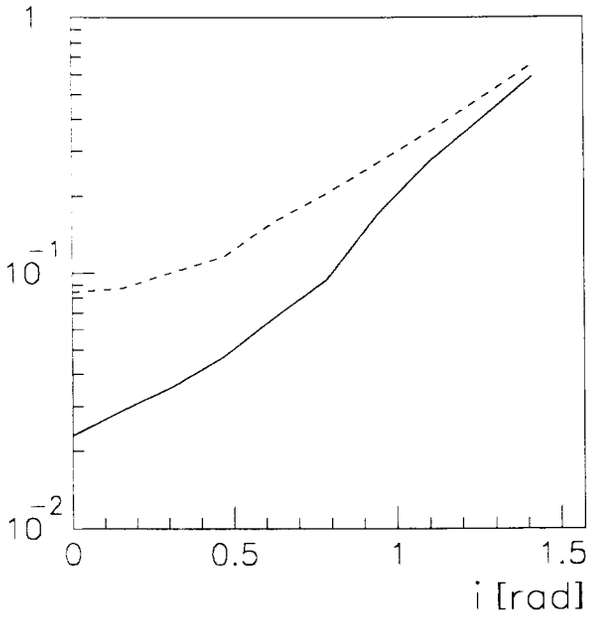

Figure 9: Back scattering probability as a function of incidence angle simulated with EGS4 (Al continuous, Fe dotted).

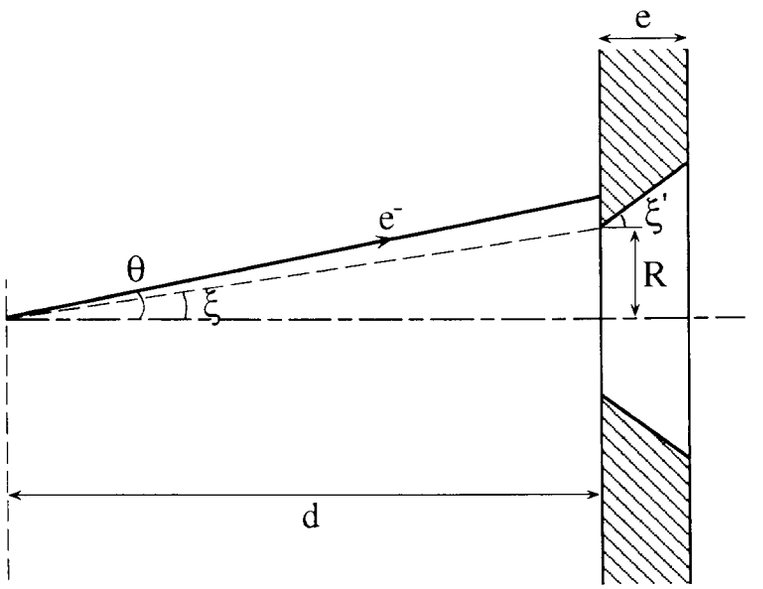

Figure 10: Schematic of a collimator (see text).

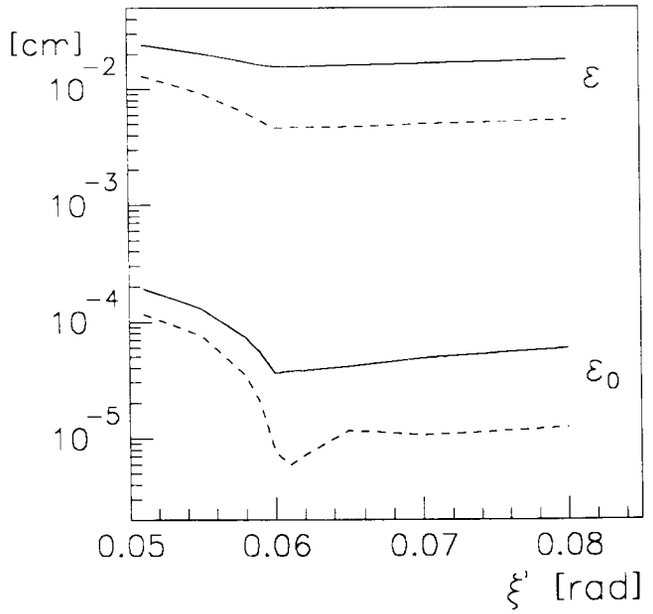

Figure 11: The variation of ε and ε_0 with ξ' (Al continuous, Fe dotted).

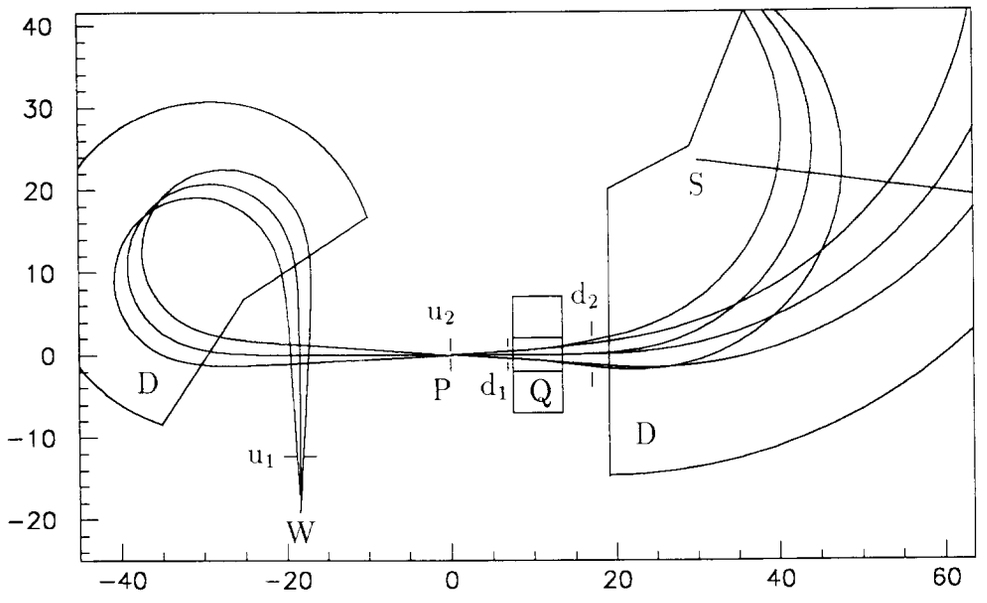

Figure 12: Schematic of the collimation systems. W: entrance window, u: upstream, d: downstream, D: dipole, Q: quadrupole, P: plasma, S: slit. The marginal rays are at ±60 mrad. Behind the plasma, 3 MeV and 6 MeV tracks are drawn. Units are centimetres.

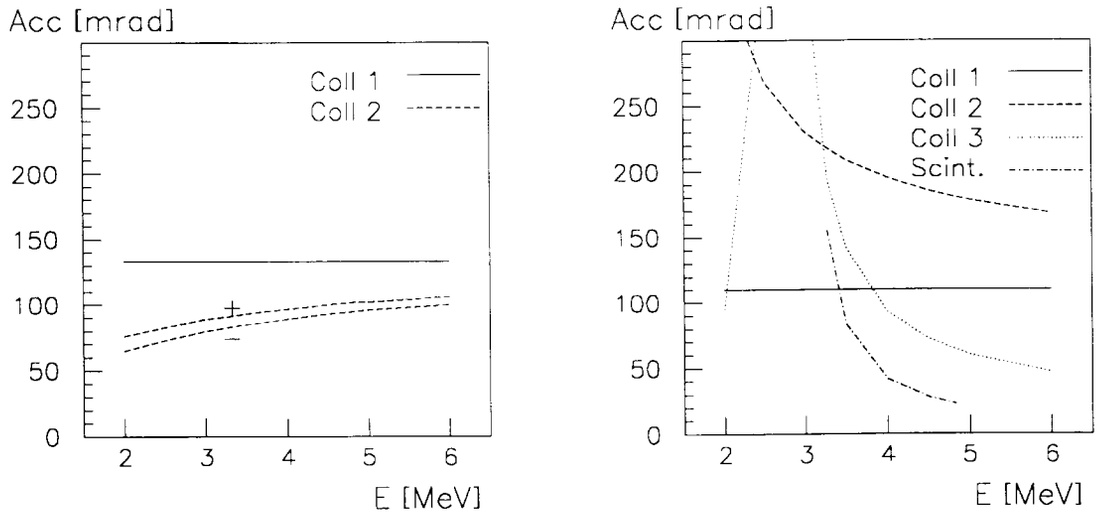

(a) Horizontal plane.

(b) Vertical plane.

Figure 13: The angular acceptance as a function of the energy of the accelerated electrons. The cut in the horizontal plane depends slightly on the sign of the angle $(+,-)$ because of the fringe field of the dipole.

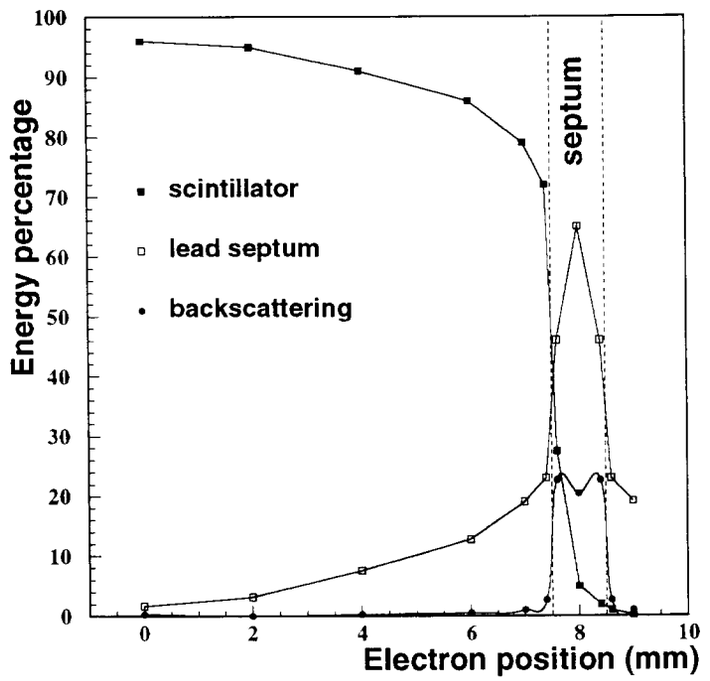

Figure 14: Percentage of lost energy as a function of the impact position of the electron.

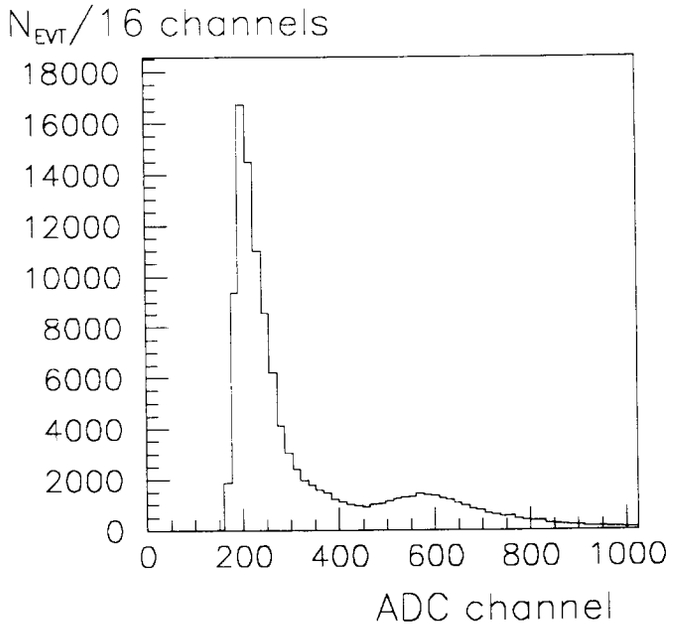

Figure 15: Cosmic muon spectrum, measured with HV=900V and amplifier gain 14.

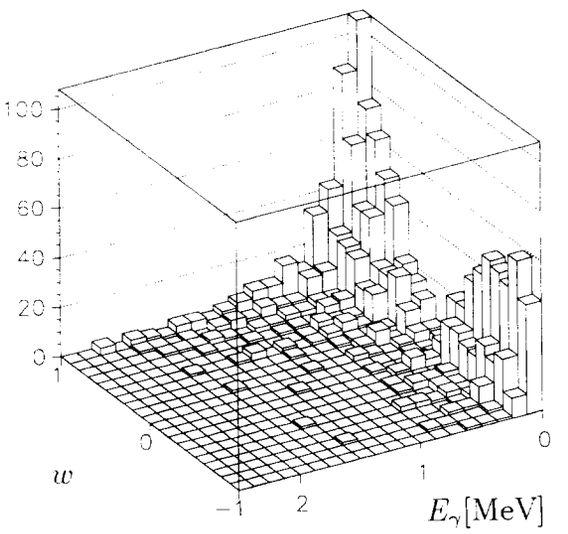

Figure 16: Emission of γ's from the dump as a function of energy and of the cosine w of the emission angle.

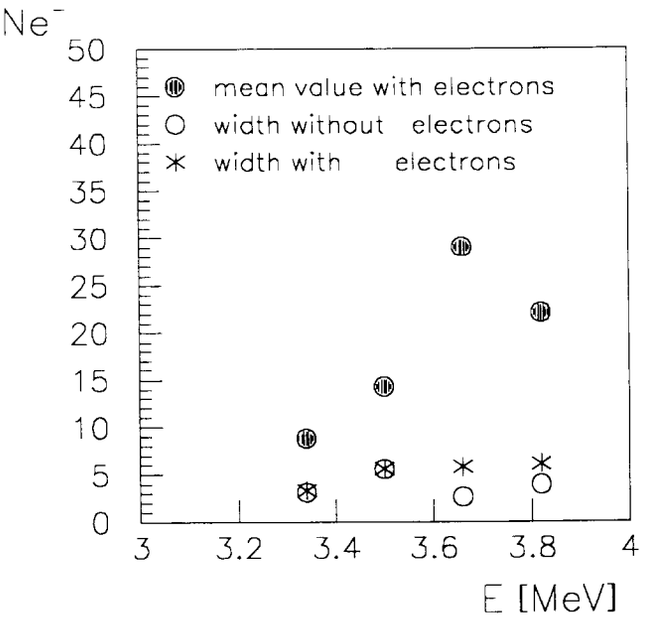

Figure 17: Pedestal mean value (with e^-) and widths (with and without e^-) of the first four channels.

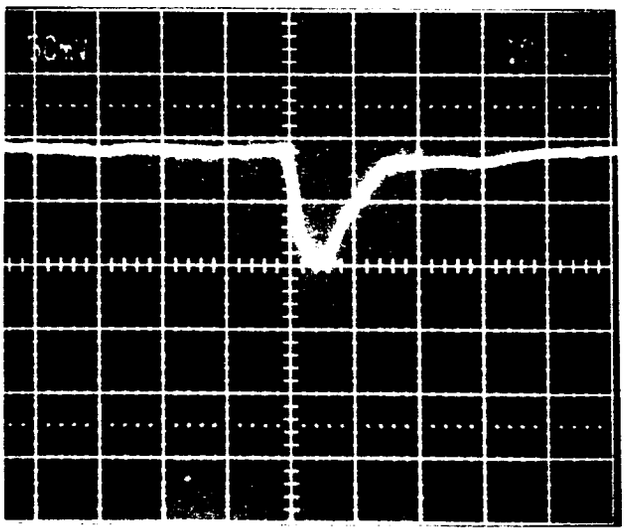

Figure 18: Oscilloscope recording of an event (shot 36, channel 2, 10 ns×50 mV per square).

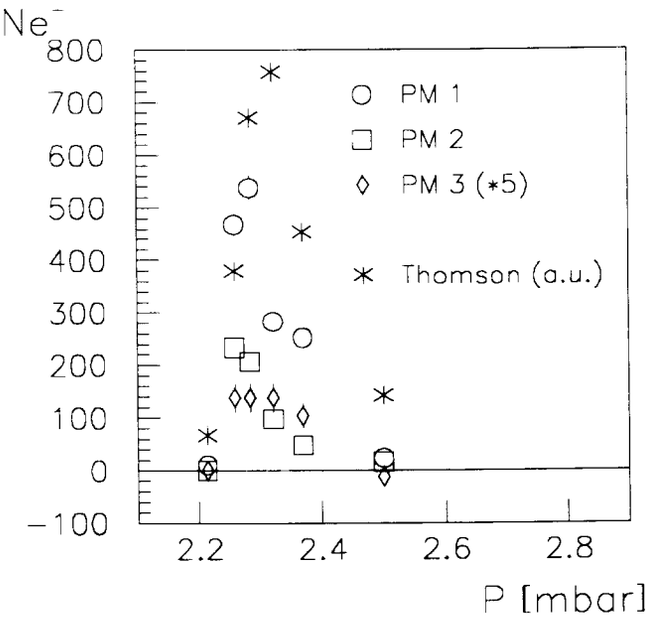

Figure 19: Number of accelerated electrons as a function of the gas pressure (at 28.7^0C).

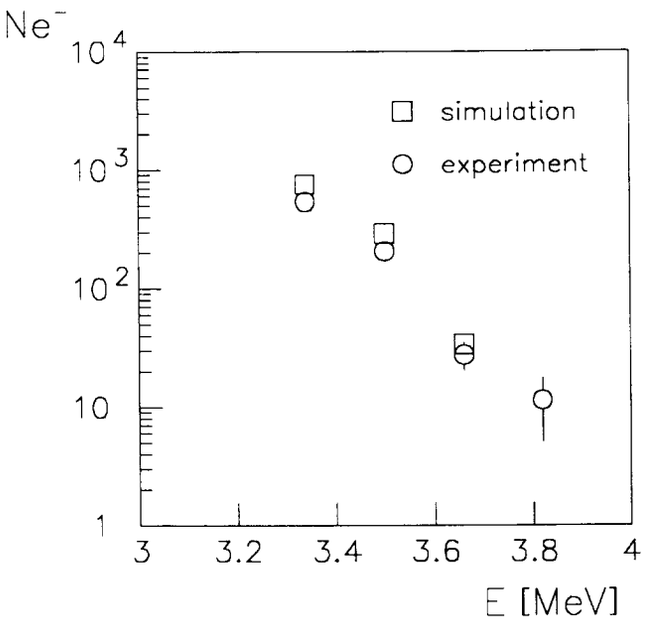

Figure 20: Measured energy spectrum and simulation (shot #36).